Journal of
Synchrotron
Radiation

ISSN 1600-5775

Received 5 August 2013
Accepted 22 October 2013

Design of an ultrahigh-energy-resolution and wide-energy-range soft X-ray beamline

L. Xue,[a] R. Reininger,[b] Y.-Q. Wu,[a] Y. Zou,[a] Z.-M. Xu,[a] Y.-B. Shi,[c] J. Dong,[c] H. Ding,[c] J.-L. Sun,[d] F.-Z. Guo,[e] Y. Wang[a]* and R.-Z. Tai[a]*

[a]Shanghai Institute of Applied Physics, Chinese Academy of Sciences, Shanghai 201800, People's Republic of China, [b]Advanced Photon Source, Argonne National Laboratory, Argonne, IL 06439, USA, [c]Institute of Physics, Chinese Academy of Sciences, Beijing 100190, People's Republic of China, [d]Dalian Institute of Chemical Physics, Chinese Academy of Sciences, Dalian 116023, People's Republic of China, and [e]Dalian Jiaotong University, Shahekou, Dalian, People's Republic of China. *E-mail: wangyong@sinap.ac.cn, tairenzhong@sinap.ac.cn

A new ultrahigh-energy-resolution and wide-energy-range soft X-ray beamline has been designed and is under construction at the Shanghai Synchrotron Radiation Facility. The beamline has two branches: one dedicated to angle-resolved photoemission spectroscopy (ARPES) and the other to photoelectron emission microscopy (PEEM). The two branches share the same plane-grating monochromator, which is equipped with four variable-line-spacing gratings and covers the 20–2000 eV energy range. Two elliptically polarized undulators are employed to provide photons with variable polarization, linear in every inclination and circular. The expected energy resolution is approximately 10 meV at 1000 eV with a flux of more than 3×10^{10} photons s^{-1} at the ARPES sample positions. The refocusing of both branches is based on Kirkpatrick–Baez pairs. The expected spot sizes when using a 10 µm exit slit are 15 µm × 5 µm (horizontal × vertical FWHM) at the ARPES station and 10 µm × 5 µm (horizontal × vertical FWHM) at the PEEM station. The use of plane optical elements upstream of the exit slit, a variable-line-spacing grating and a pre-mirror in the monochromator that allows the influence of the thermal deformation to be eliminated are essential for achieving the ultrahigh-energy resolution.

Keywords: soft X-ray beamline; ultrahigh-energy resolution; ARPES; thermal deformation.

1. Introduction

Angle-resolved photoemission spectroscopy (ARPES) (Hüfner, 2003) and photoemission electron microscopy (PEEM) (Scholl, 2003) are two powerful experimental technologies based on the photon-in/electron-out principle. With its ability to probe directly the electronic band structure in the momentum space, ARPES is an indispensable tool for research on complex systems such as high-temperature superconductors (Damascelli *et al.*, 2003; Richard *et al.*, 2011), spin electronics materials (Souma *et al.*, 2010), topological insulators (Hasan & Kane, 2010) and diluted semiconductors (Richard *et al.*, 2012). The escape length of photoelectrons in solids within the widely used energy range between 10 eV and 200 eV (VUV) is only a few angstroms (Kobayashi *et al.*, 2012), implying that ARPES experiments in this regime are highly surface sensitive. To probe the bulk of materials it is necessary to excite either with longer wavelength radiation or with soft X-rays, which are both characterized by much larger escape depths. Although high-energy resolution is easily achieved at longer wavelengths, the portion of momentum space that can be probed is limited and often smaller that the size of the Brillouin zone of typical materials. In contrast to low photon energy, soft X-rays from synchrotron radiation with energy around 1000 eV allow bulk-sensitive measurements covering the full Brillouin zone. However, the energy resolution is much lower than in the VUV range, *e.g.* the highest energy resolution at the ADRESS beamline (Strocov *et al.*, 2010) is 30 meV at 1000 eV.

PEEM is a useful surface probe technique capable of detecting changes in the local work function of the sample surface *in situ* and in real time. It can also provide valuable information on reaction dynamics (Bauer, 1994). The combined use of PEEM and X-rays (XPEEM) with synchrotron radiation widens the PEEM application fields and provides a powerful means for research and development in surface science and nanotechnology (Locatelli & Bauer, 2008). The energy range between ~100 and 2000 eV spans the absorption edges of many important elements. *K*-edges of light elements from C to Si, *L*-edges of transition metals from Ti to Zn and of main group elements from Ca to Br, and *M*-edges of rare-earth metals from La to Yb can be studied with soft X-rays. The important magnetic elements, the transition metals Cr, Mn, Fe, Co and Ni and the rare-earth metals Sm, Eu, Gd and Tb have absorption edges between 570 and 1300 eV, at which magnetism can be measured easily by XPEEM (Feng & Scholl, 2007). The unique characteristics of X-ray radiation from third-generation synchrotron radiation sources further enhances PEEM in spectromicroscopy.

Table 1
Main parameters of the storage ring and of the two EPUs.

Beam current (mA)	300
σ_x (μm)	159
σ_y (μm)	9.9
$\sigma_{x'}$ (μrad)	33
$\sigma_{y'}$ (μrad)	3.9
LEID period length (mm)	148
LEID number of periods	32
LEID total length (m)	4.736
LEID energy range (eV)	20–200
HEID period length (mm)	58
HEID number of periods	84
HEID total length (m)	4.872
HEID energy range (eV)	200–2000

A new soft X-ray beamline is under construction at the Shanghai Synchrotron Radiation Facility (SSRF) covering the energy range between 20 and 2000 eV with an improved energy resolution of ∼10 meV at 1000 eV. This beamline will make use of the advantages of synchrotron radiation from insertion devices, such as its high brightness, wide tunability and polarization, for research using ARPES and PEEM. The design of this beamline is described below.

2. Beamline

2.1. Source

The SSRF is a 3.5 GeV third-generation synchrotron radiation facility with 3.9 nm rad emittance (Xu & Zhao, 2008). Although the beam current of the storage ring is presently 200 mA, the design of the beamline is for 300 mA since the beam current will be upgraded to this value in the near future. In order to optimize the flux and control the emitted power over the wide energy range covered by the beamline, 20–2000 eV, two elliptical polarized undulators (EPUs) are used. The high-energy insertion device (HEID) will cover the energy range 200–2000 eV, and the low-energy insertion device (LEID), which is quasi-periodic to suppress the high-order undulator harmonics, will cover the 20–200 eV range. The two undulators are side-by-side in the straight section and can be easily switched without damping the electron beam. The main parameters of the two EPUs are listed in Table 1. The flux emitted in the central cone by the two devices calculated using the *SPECTRA* code (Tanaka & Kitamura, 2001) is shown in Fig. 1. In the calculation we have assumed ideal insertion devices; the quasi-periodicity will reduce the flux by 10–20%. The calculated maximum total power emitted from the HEID is slightly less than 7 kW.

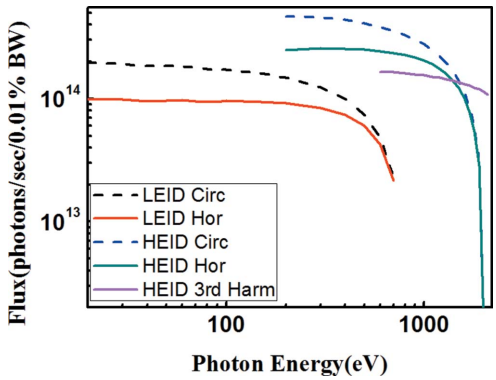

Figure 1
Linearly (solid lines) and circularly (dash lines) polarized flux emitted by two EPUs.

Table 2
Key optical parameters of elements in the optical scheme.

Element	Shape	Deflection/angle (°)	Coating	Slope error (μrad)†
M1‡	Plane	Horizontal/2.4	Au	0.7/5
M2‡	Plane	Vertical/variable	Ni/Au	0.2/2
LEG§ 400 lines mm^{-1}	Plane	Vertical/variable	Au	0.2/2
MEG§ 800 lines mm^{-1}	Plane	Vertical/variable	Ni	0.2/2
HEG§ 1200 lines mm^{-1}	Plane	Vertical/variable	Au	0.2/2
VEG§ 3600 lines mm^{-1}	Plane	Vertical/variable	Au	0.1/2
Slit (ARPES)§				
M3	Elliptical cylindrical	Horizontal/3	Au	2/5
M4	Elliptical cylindrical	Vertical/2.5	Au	0.8/5
Sample (ARPES)				
Mb	Plane	Horizontal/3.5	Au	0.7/5
Slit (PEEM)§				
M3b	Elliptical cylindrical	Vertical/2.5	Au	0.8/5
M4b	Elliptical cylindrical	Horizontal/3	Au	2/5
Sample (PEEM)				

† Meridional/sagittal. ‡ Internally water cooled. § Water cooled.

2.2. Beamline

The beamline layout is shown in Fig. 2. Table 2 summarizes the optical components as well as the assumed RMS slope errors on the optics. The optical design has been optimized for the ARPES branch as it is the most demanding experiment at the SSRF. The two beamline branches will work in a time-shared mode by switching the plane mirror Mb (see Fig. 2).

Ultrahigh-energy resolution is the main goal of this beamline. To accomplish this, we avoid non-planar elements upstream of the exit slits. A plane mirror, M1, whose main function is to absorb the heat load and to suppress the high-order harmonics, is mounted before the monochromator deflecting the beam in the horizontal direction. The angle of incidence on M1 was chosen to be 1.2° as a compromise between high reflectivity at high photon energies and filtering the

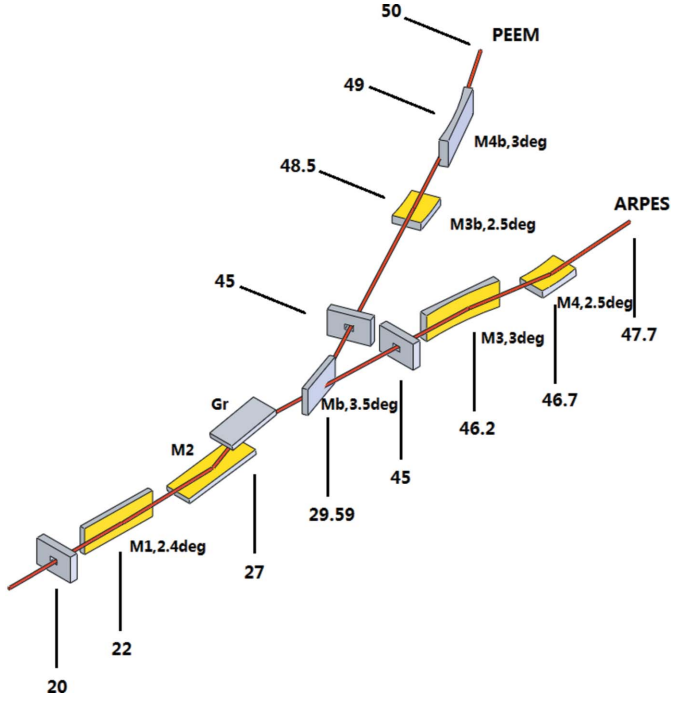

Figure 2
Beamline layout. The distances (in meters) are from the center of the insertion device.

power transmitted to the downstream optical elements. An internal water-cooling scheme was adopted for M1 to minimize the effects of the absorbed power on this mirror that can be as high as 2 kW.

The core instrument of the beamline is a vertically dispersing variable-included-angle variable-line-spacing plane-grating monochromator (VPGM) (Reininger, 2011) equipped with four gratings. Each grating is optimized for energy resolution and/or flux covering a specific energy range. The pre-mirror (M2) needs to be translated and rotated in order to illuminate the grating with the correct angle of incidence that will keep the beam in focus at the exit slit. The translation and rotation are actually achieved by a simple rotation (Riemer & Torge, 1983). The pre-mirror has two different reflective coatings side-by-side: Au and Ni. Ni is used with the low-energy grating (LEG) and with the middle-energy grating (MEG), whereas Au is used with the high-energy grating (HEG) and with the very high resolution energy gratings (VEGs). The line density at the center of each grating is shown in Table 2.

Kirkpatrick & Baez (KB) systems (Kirkpatrick & Baez, 1948) based on elliptical cylinder mirrors are used to focus the beam onto the two experimental stations. The vertically focusing mirror images the vertical exit slit whereas the horizontally focusing mirror images the source along the horizontal direction.

3. Expected performance

3.1. Energy resolution

The main optical aberrations degrading the resolution of a grating monochromator can be minimized by using a line density variation on the grating given by

$$k(w) = k_0\left(1 + 2b_2 w + 3b_3 w^2 + \ldots\right) \tag{1}$$

where k_0 is the line density at the grating center and w is the coordinate along the grating length.

The defocus term in the optical path function given by

$$F_{20} = \frac{\cos^2\alpha}{r_1} + \frac{\cos^2\beta}{r_2} - 2b_2 nk_0\lambda \tag{2}$$

can be zeroed at one wavelength by solving (2) where λ is the wavelength, α and β are the incident and diffraction angles, n is the diffraction order, r_1 is the distance from the source to the grating and r_2 is the distance from the grating to the exit slit.

In the present design [see Reininger (2011) and references therein] F_{20} can be zeroed for all wavelengths covered by the grating by solving simultaneously the grating equation and equation (2) after a suitable choice of b_2. This yields a unique pair of α and β for each photon energy and grating. The fixed-focus constant $c_{\rm ff}$ value ($\cos\beta/\cos\alpha$) as a function of photon energy for each of the gratings is approximately constant and equal to 2.2 for the LEG, MEG and HEG, and to 7 for the VEG.

The coma term in the optical path function given by

$$F_{30} = \sin\alpha\ \frac{\cos^2\alpha}{r_1^2} + \sin\beta\ \frac{\cos^2\beta}{r_2^2} - 2b_3 nk_0\lambda \tag{3}$$

can also be zeroed at a single wavelength; nevertheless, the effect of the coma aberration over the energy covered by each grating is negligible compared with the resolution terms described in the equations below.

Consequently, the energy resolution in this design is determined by four factors: source size, exit slit size, meridian slope error of the grating and plane mirror. Their contributions to the total energy resolution $\Delta E_{\rm total}$ are

$$\begin{aligned}
\Delta E_{\rm so} &= \frac{2.7\Sigma_y\cos(\alpha)E}{nkr_1\lambda},\\
\Delta E_{\rm ex} &= \frac{s\cos(\beta)E}{nkr_2\lambda},\\
\Delta E_{\rm gr} &= \frac{5.4\sigma_{\rm gr}E}{nk\lambda}\cos\left(\frac{\alpha+\beta}{2}\right)\cos\left(\frac{\alpha-\beta}{2}\right),\\
\Delta E_{\rm pm} &\simeq \frac{5.4\sigma_{\rm pm}\cos(\alpha)E}{nk\lambda},\\
\Delta E_{\rm total} &= \left(\Delta E_{\rm so}^2 + \Delta E_{\rm ex}^2 + \Delta E_{\rm gr}^2 + \Delta E_{\rm pm}^2\right)^{1/2},
\end{aligned} \tag{4}$$

where Σ_y is the RMS value of the source size, E is the photon energy, $\sigma_{\rm gr}$ and $\sigma_{\rm pm}$ are the meridian RMS slope errors of the grating and plane mirror, respectively, and s is the exit slit size.

The individual terms as well as the total energy resolution for each of the four gratings are shown in Fig. 3. The assumed slit sizes and slope errors used in the calculations are given in the figure caption. For the LEG and MEG, the largest contribution to the energy resolution is due to the source size and the exit slit size. In order to achieve 10 meV energy resolution at 1000 eV, a VEG is used. In this case the effect of the grating slope error is the second largest and becomes more significant at higher photon energies. Actually, this is

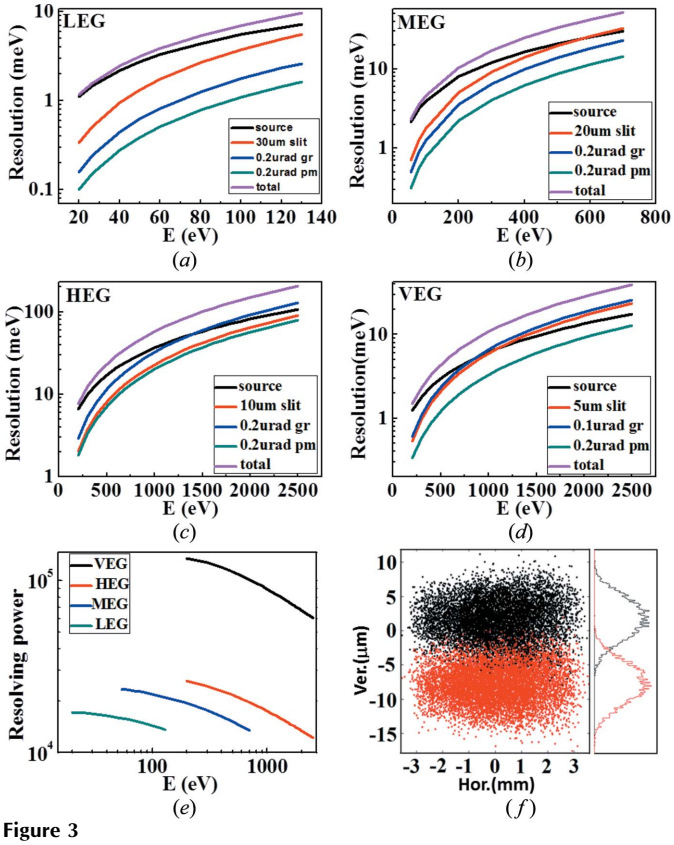

Figure 3
Terms contributing to the energy resolution and total energy resolution in each of the four gratings. (*a*) Resolution due to a 30 μm exit slit and meridional RMS slope errors of 0.2 μrad on M2 and LEG grating. (*b*) Resolution due to a 20 μm exit slit and meridional RMS slope errors of 0.2 μrad on M2 and MEG grating. (*c*) Resolution due to a 10 μm exit slit and meridional RMS slope errors of 0.2 μrad on M2 and HEG grating. (*d*) Resolution due to a 5 μm exit slit and meridional RMS slope errors of 0.2 μrad on M2 and 0.1 μrad on VEG grating. (*e*) The total resolving power of four gratings with slit sizes listed in (*a*)–(*d*). (*f*) Spot pattern at the exit plane for 1000 eV and 1000.011 eV with VEG.

also the case for the HEG, which has 1200 lines mm^{-1} to obtain a balance between high flux and high energy resolution but not ultra-high energy resolution. The required RMS slope error of the VEG is 0.1 µrad, which is achievable for plane optics with the required length (∼120 mm). Fig. 3(*e*) shows the expected resolving power achievable with each grating used with the parameters given in Figs. 3(*a*)–3(*d*).

The resolution can be verified by ray tracings, which were carried out using the *SHADOW* code (Welnak *et al.*, 1994) including the same RMS slope errors as in the analytical calculations. As an example we show in Fig. 3(*f*) the spot pattern at the exit slit plane for 1000 eV and 1000.011 eV when using the VEG and with the monochromator tuned to 1000 eV. As seen in the figure, the two energies are well separated showing a resolution better than 11 meV. The value in Fig. 3(*d*) is slightly worse since it includes the contribution from a 5 µm exit slit.

3.2. Photon flux

The reflectivities of all mirrors were calculated using the data compiled by Palik (1991) for photon energies lower than 30 eV and the optical constants in the Henke tables (Henke *et al.*, 1993) at higher photon energies. The surface roughness of all the optical elements is assumed to be 0.3 nm. The gratings' efficiencies were calculated using Neviere's code (Nevière *et al.*, 1974) assuming they have constant groove densities and using holographic gratings.

The photon flux expected at the ARPES station for linear and circular polarizations with two EPUs is presented in Fig. 4. Slightly smaller values are expected at the PEEM station since it requires one more reflection. There is a flux increase when switching from the LEID to the HEID at 200 eV. As seen in the figure, the calculated flux at the sample is higher than 2×10^{12} photons s^{-1} up to 1.3 keV with the LEG, MEG, HEG and a bandwidth of 0.01%. When switching to VEG, the flux expected at 1 keV for horizontal linear polarization at a resolution of 11 meV is about 3×10^{10} photons s^{-1}.

3.3. Spot size

Two different KB systems based on elliptical cylinder mirrors are used to focus the beam at the two experimental stations. In the ARPES KB system the first mirror (M3) focuses the source along the horizontal direction and the second mirror (M4) focused the secondary source (exit slit) along the vertical direction onto the sample. The ray-tracings result (Fig. 5*a*) shows that the spot size is 15 µm × 4.7 µm (FWHM) at the sample of the ARPES station at 1000 eV using the VEG and a 10 µm exit slit. The slope errors on the

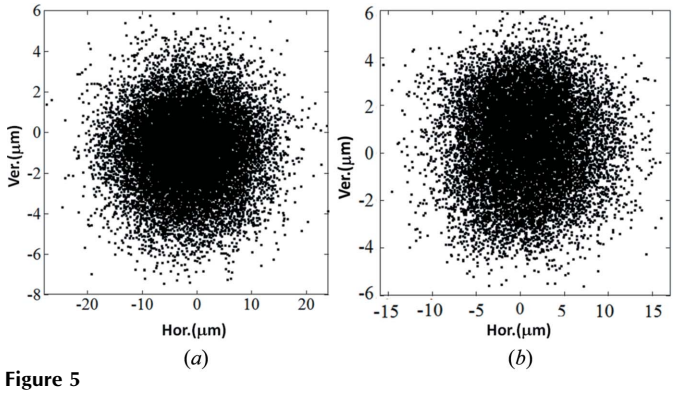

Figure 5
(*a*) Spot size at the sample position of the ARPES station for 1000 eV using the VEG with 10 µm exit slit. (*b*) Spot size at the sample position of the PEEM station for 1000 eV using the VEG with 10 µm exit slit.

optical elements listed in Table 2 are included in the ray tracings. To reduce the spot size at the sample of the PEEM station, the first mirror (M3b) in the PEEM KB system is the vertical focusing mirror and the second one is the horizontal focusing mirror. In addition, the distance between the exit slit and the first mirror is also increased to 3.5 m for the same purpose. The spot size at the sample of the PEEM station (see Fig. 5*b*) is 9.9 µm × 4.8 µm (FWHM). The ray tracings in Fig. 5(*b*) were also performed using a 10 µm exit slit and the slope errors listed in Table 2.

4. Thermal correction

4.1. Thermal deformation correction

The deformation of the mirrors' figure due to the absorbed heat load can significantly impair the beamline performance. Deformations along the meridional direction on M1 and the sagittal direction on M2 will affect the horizontal spot size whereas those along the sagittal direction on M1 and along the meridional direction along M2 will affect the monochromator resolution. Thus, we studied the thermal deformation on the M1 and M2 mirrors with finite-element analysis (FEA), since these mirrors absorb most of heat load in the beamline.

4.1.1. Thermal deformation on M1. The maximum calculated power and power density absorbed by M1 will be up to 2 kW and 1.1 W mm^{-2} at 200 eV in vertical polarization (under the lowest gap of HEID). Fig. 6 shows the absorbed power density by M1. The beamline aperture is 400 µrad in both directions.

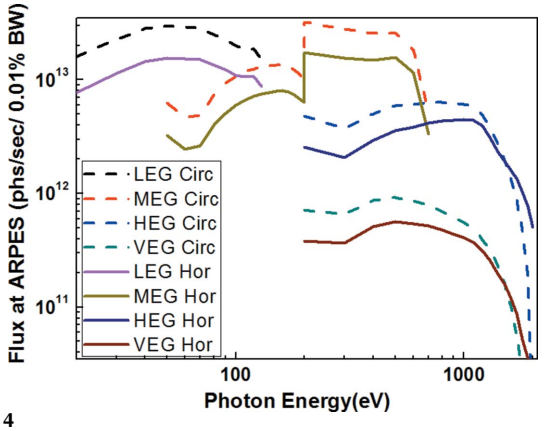

Figure 4
Photon flux at the ARPES sample at a 'resolving power' of 10^4 for horizontal (solid traces) and circular (dash traces) polarizations.

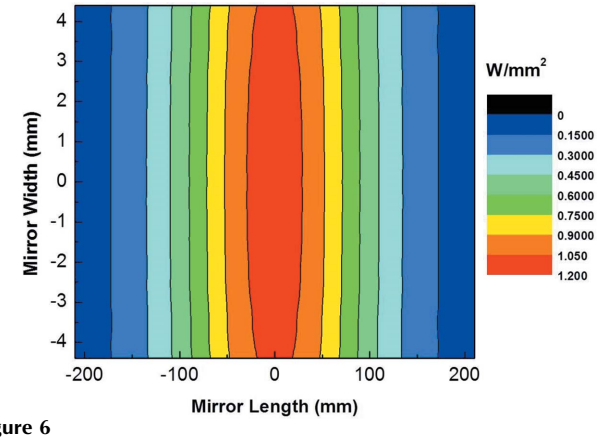

Figure 6
Power density absorbed by M1 when HEID is tuned to emit 200 eV photons in vertical polarization.

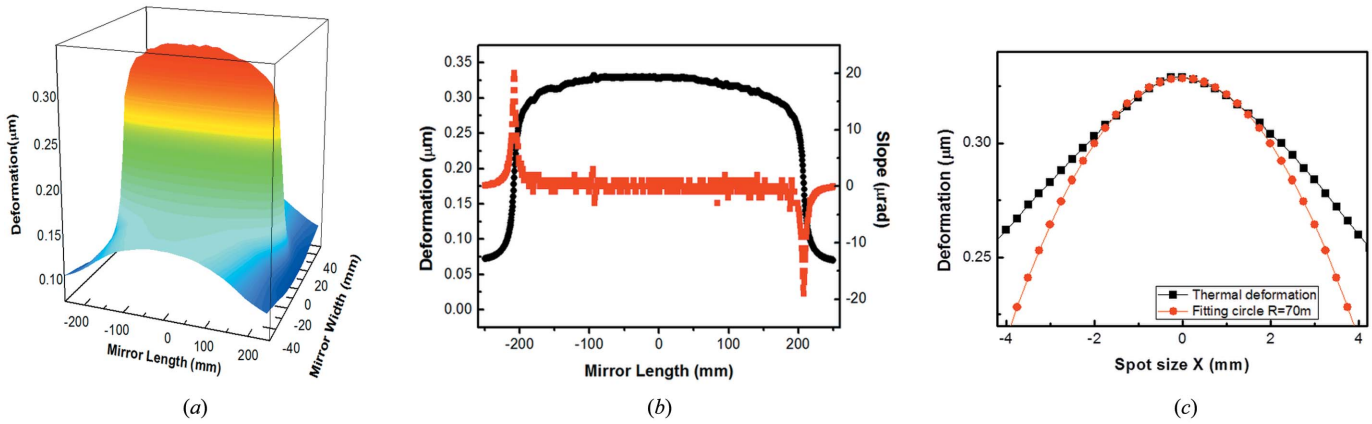

(*a*) (*b*) (*c*)

Figure 7
Thermal deformation distribution on the surface of M1 using the HEID when tuned to emit 200 eV in vertical polarization. (*b*) Thermal deformation distribution (black curve) and slope error (red curve) on the middle of M1 along the meridional direction. (*c*) Thermal deformation distribution (black curve) and circular fitting (red curve) on the middle of M1 along the sagittal direction and fit with a 70 m radius.

A direct micro-channel cooling model is used in M1 and is currently being procured. The assumed film coefficient is 0.01 W mm^{-2} K^{-1} and the cooling temperature is 303 K. The channel period is 2.5 mm with a channel height and width of 5 mm and 1 mm, respectively.

The FEA result is shown in Fig. 7(*a*). The deformation of M1 along the meridional direction at ±190 mm is equivalent to a convex mirror with a 5.7 × 10^5 m radius of curvature and is almost linear [red line, as seen in Fig. 7(*b*)]. The effect of the convex mirror on the beam is equivalent to increasing the horizontal divergence angle of the source, which decreases the object distance of the M3 mirror from the design value of 46.2 m to 46.12 m. This will increase the horizontal spot size from 12.1 μm (FWHM) to 12.2 μm (FWHM) obtained by ray tracing at the ARPES sample position, which is small enough to be negligible.

The thermal deformation along the sagittal direction can be fitted over the central part with a circle of 70 m radius (see Fig. 7*c*). Therefore, the M1 mirror could be approximately treated as a convex cylindrical mirror with a 70 m convex radius.

Fig. 8(*a*) shows the ray tracings at the exit slit plane for 200.00 eV and 200.002 eV performed when the VEG is tuned to 200 eV. These results should be compared with those shown in Fig. 8(*b*) in which we have included the deformation of M1 using the pre-surface routine in *SHADOW*. As seen in the figures, the thermal deformation of M1 has practically no effect on the energy resolution.

4.1.2. Thermal deformation on M2. M2 will have the same internal micro-channel water-cooling system as described for M1. The absorbed heat load on M2 when using the VEG and when the HEID source is tuned to emit vertical polarized radiation at 1000 eV is shown in Fig. 9. Evidently the beam is not at the mirror length center of M2 due to its mechanical arrangement (Riemer & Torge, 1983). The shift in the mirror width is because we were using an Au stripe. The maximum calculated power and power density absorbed under these conditions are 187 W and 0.21 W mm^{-2}, respectively. The mirror deformation and a cut along the meridional direction are shown in Figs. 10(*a*) and 10(*b*), respectively.

As explained above for the M1 case, the effect of thermal deformation along the sagittal direction can be approximated as a convex

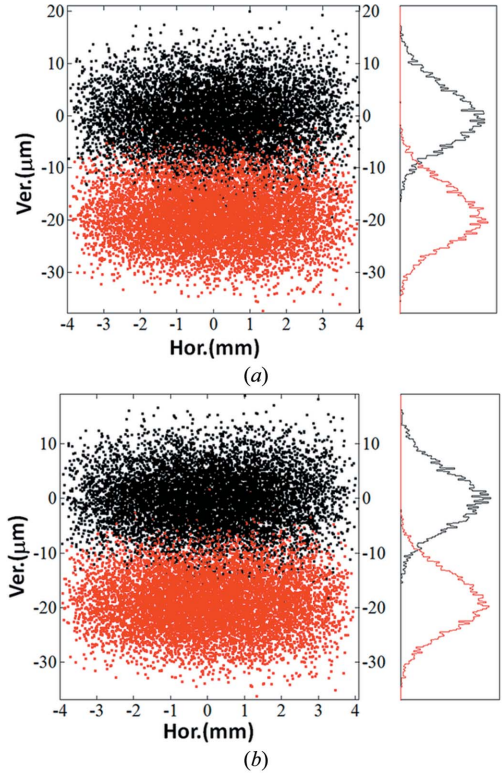

(*a*)

(*b*)

Figure 8
Ray tracings at the exit slit plane for 200.00 eV and 200.002 eV (*a*) without thermal deformation on M1 and (*b*) with thermal deformation.

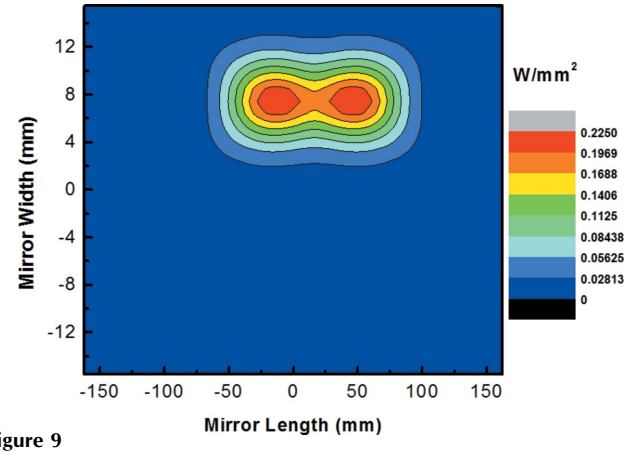

Figure 9
Heat load distribution on the surface of M2 when using the VEG grating and the HEID source tuned to emit vertical polarization at 1000 eV.

mirror. A fit to the sagittal slope over the dimension illuminated by the central cone radiation yields a convex radius of curvature of 22 m. This will increase the horizontal spot size from 12.1 µm (FWHM) to 13.6 µm (FWHM) obtained by ray tracing at the ARPES sample position.

The meridional thermal deformation of M2 over the central part can be approximated by a convex radius of 3.6 km (see Fig. 10*b*). This radius means that the distance between the source and the grating will decrease from 27.0 m to 26.3 m. However, this monochromator design (Reininger *et al.*, 2008) allows this effect to be compensated for by changing the c_{ff} value.

Actually, it can be seen from Fig. 10(*b*) that the thermal deformation cannot be fitted perfectly by a constant radius of curvature. In order to achieve the ultimate energy resolution, an aperture will be positioned after the monochromator. This will cause a 28% loss in flux and a negligible resolution degradation (a few percent) due to the reduction on the number of illuminated grooves.

Figs. 11(*a*) and 11(*b*) illustrate the effect of the thermal deformation at the exit plane at 1000.00 eV and 1000.011 eV, respectively. The results in the right-hand panel were obtained by including the FEA of M2 in the ray tracings. Clearly, the heat-induced deformation of M2 has a major effect on the energy resolution. Fig. 11(*c*) shows the significant improvement obtained by changing the c_{ff} value from 7 to 7.363. A comparison with Fig. 11(*a*) clearly shows some scatter at the edge of the beams affecting the energy resolution. The scattered rays are absent in Fig. 11(*d*) which was obtained by limiting the beam to the central 64%. Evidently the effect of the diffraction is not present in the ray tracings, but, as mentioned above, its effect on the total resolution is relatively small.

With this monochromator setting and EPU tuning, the grating absorbs less than 1 W with a maximum absorbed power density of less than 3 mW mm^{-2}. The resulting slight thermal deformation can be neglected.

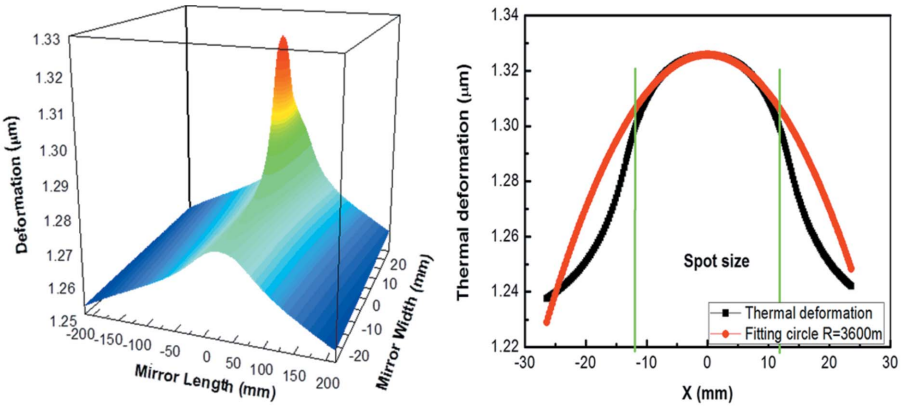

Figure 10
(*a*) Thermal deformation distribution of M2 when using the VEG grating and when the HEID source is tuned to emit vertical polarized radiation at 1000 eV. (*b*) Cut along the meridional direction and fit with a 3600 m radius. The vertical lines (green lines) show the spot size of the central cone on M2.

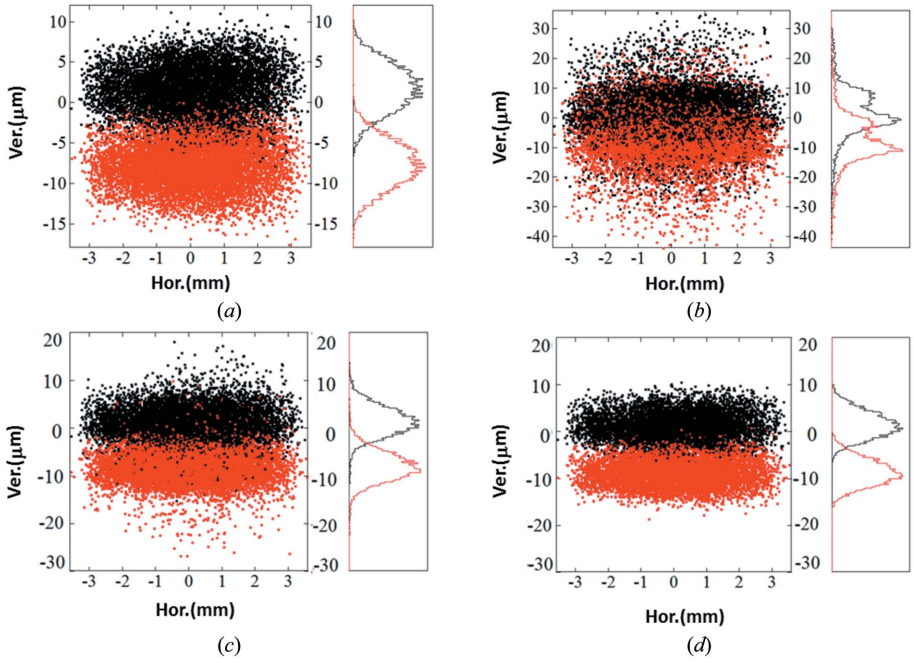

Figure 11
Ray tracings at the exit slit plane for 1000 eV and 1000.011 eV. (*a*) No thermal deformation. (*b*) With thermal deformation. (*c*) As in (*b*) with c_{ff} correction. (*d*) As in (*c*) after aperturing the beam.

5. Conclusion

A new soft X-ray beamline with ultrahigh energy resolution and wide energy range has been designed and is currently under construction at SSRF. The use of two EPUs, interchangeable without damping the electron beam, will deliver circular (and linear) polarization from 20 eV to almost 2 keV. A plane-grating monochromator equipped with four VLS gratings will allow very high flux and/or very high resolving power to be obtained. A resolving power of 10^5 at 1000 eV will be achieved using a high-line-density grating and the thermal correction possible in this monochromator design. This beamline will start commissioning at the end of 2013 and its two branches will allow novel ARPES and PEEM experiments.

This work has been supported by the Major Scientific Equipment Project 'Photoemission instrument with ultrahigh energy resolution and wide energy range', the National Natural Science Foundation of China (No. 11005146) and the Open Research Project of Large Scientific Facility from Chinese Academy of Sciences 'Study on self-assembly technology and nanometer array with ultrahigh density'. We would like to acknowledge Dr Y. F. Hu (Canadian Light Source), Dr M. Shi, Dr V. N. Strocov and U. Flechsig (Paul Scherrer Institut), Professor Y. L. Yan and Professor H. J. Qian (Institute of High Energy Physics) for beneficial discussions.

References

Bauer, E. (1994). *Rep. Prog. Phys.* **57**, 895–938.
Damascelli, A., Hussain, Z. & Shen, Z.-X. (2003). *Rev. Mod. Phys.* **75**, 473–541.
Feng, J. & Scholl, A. (2007). *Photoemission Microscopy*, in *Science of Microscopy*, edited by P. W. Hawkes and J. C. H. Spence, pp. 657–695. Berlin: Springer.

Hasan, M. Z. & Kane, C. L. (2010). *Rev. Mod. Phys.* **82**, 3045–3067.
Henke, B. L., Gullikson, E. M. & Davis, J. C. (1993). *At. Data Nucl. Data Tables*, **54**, 181–342.
Hüfner, S. (2003). *Photoelectron Spectroscopy: Principles and Applications*, 3rd ed. Berlin: Springer-Verlag.
Kirkpatrick, P. & Baez, A. V. (1948). *J. Opt. Soc. Am.* **38**, 766–774.
Kobayashi, M., Muneta, I., Schmitt, T., Patthey, L., Ohya, S., Tanaka, M., Oshima, M. & Strocov, V. N. (2012). *Appl. Phys. Lett.* **101**, 242103.
Locatelli, A. & Bauer, E. (2008). *J. Phys. Condens. Matter*, **20**, 093002.
Nevière, M., Vincent, P. & Petit, R. (1974). *Nouv. Rev. Opt.* **5**, 65–77.
Palik, E. (1991). *Handbook of Optical Constants of Solids.* New York: Academic Press.
Reininger, R. (2011). *Nucl. Instrum. Methods Phys. Res. A*, **649**, 139–143.
Reininger, R., Kriesel, K., Hulbert, S. L., Sánchez-Hanke, C. & Arena, D. A. (2008). *Rev. Sci. Instrum.* **79**, 033108.
Richard, P., Sato, T., Nakayama, K., Takahashi, T. & Ding, H. (2011). *Rep. Prog. Phys.* **74**, 124512.
Richard, P., Sato, T., Souma, S., Nakayama, K., Liu, H. W., Iwaya, K., Hitosugi, T., Aida, H., Ding, H. & Takahashi, T. (2012). *Appl. Phys. Lett.* **101**, 232105.
Riemer, F. & Torge, R. (1983). *Nucl. Instrum. Methods*, **208**, 313–314.
Scholl, A. (2003). *Curr. Opin. Solid State Mater. Sci.* **7**, 59–66.
Souma, S., Takayama, A., Sugawara, K., Sato, T. & Takahashi, T. (2010). *Rev. Sci. Instrum.* **81**, 095101.
Strocov, V. N., Schmitt, T., Flechsig, U., Schmidt, T., Imhof, A., Chen, Q., Raabe, J., Betemps, R., Zimoch, D., Krempasky, J., Wang, X., Grioni, M., Piazzalunga, A. & Patthey, L. (2010). *J. Synchrotron Rad.* **17**, 631–643.
Tanaka, T. & Kitamura, H. (2001). *J. Synchrotron Rad.* **8**, 1221–1228.
Welnak, C., Chen, G. J. & Cerrina, F. (1994). *Nucl. Instrum. Methods Phys. Res. A*, **347**, 344–347.
Xu, H. J. & Zhao, Z. T. (2008). *Nucl. Sci. Technol.* **19**, 1–6.